A Spectral Element Eulerian-Lagrangian Atmospheric Model (SEELAM)

Francis X. Giraldo
Naval Research Laboratory
Monterey, CA 93943
E-mail: giraldo@nrlmry.navy.mil

A new dynamical core for numerical weather prediction (NWP) based on the spectral element Eulerian-Lagrangian (SEEL) method is presented. This paper represents a departure from previously published work on solving the atmospheric equations in that the horizontal operators are all written, discretized, and solved in 3D Cartesian space. The advantages of this new methodology are: the pole singularity which plagues all grid-point methods disappears, the horizontal operators can be approximated by local high-order elements, the Eulerian-Lagrangian formulation permits extremely large time-steps, and the fully-implicit Eulerian-Lagrangian formulation only requires the inversion of a 2D Helmholtz operator. In order to validate the SEELAM model, results for four test cases are shown. These are: the Rossby-Haurwitz waves number 1 and 4, and the Jablonowski-Williamson balanced initial state and baroclinic instability tests. Comparisons with four well-established operational models show that SEELAM is as accurate as spectral transform models.

1. INTRODUCTION

Because of the changing trends in high performance computers from large vector machines to distributed-memory architectures, numerical methods that decompose the physical domain into smaller pieces have been receiving significant attention. This new focus on local methods is especially true in the atmospheric sciences where very large models covering the entire globe are run in time-scales ranging from days (in numerical weather prediction) to thousands of years (in climate simulations). Finite difference and finite element methods are two such methods which decompose the domain locally thereby facilitating their implementation on distributed-memory computers. However, one of the biggest disadvantages of these methods is that traditionally they have not been able to compete, in terms of accuracy, with spectral transform methods which are typically used operationally in numerical weather prediction (NWP) and climate modeling. For example, spectral transform models are used by the National Center for Environmental Prediction [8], the European Centre for Medium-Range Forecasts [9], the National Center for Atmospheric Research [3], and the U.S. Navy [4].

Spectral element methods combine the local domain decomposition property of finite element methods with the high-order accuracy of spectral transform methods. In other words, spectral

elements are as local as finite element methods, and thereby can be used as efficiently on distributed-memory computers while sustaining the same level of accuracy obtained with spectral transform methods. These methods are essentially high-order finite element methods where the grid points are chosen to be the Legendre-Gauss-Lobatto (LGL) points. This choice of grid points allows for stable high-order interpolations and results in efficient numerical integration strategies because the LGL points are also used as the quadrature points in the numerical integration required by the weak integral formulation common to all Galerkin methods.

Using the spectral element method we have developed a hydrostatic primitive equation model for NWP [2]. However, in that work the time integration scheme used was an explicit Eulerian method. Although explicit time-integration methods for atmospheric simulations can be incredibly fast and quite accurate, their main disadvantage is that small time steps must be observed in order to maintain stability. The reason for this prohibitively small time-step is due to the fast moving gravity waves. These waves require a small time-step while only carrying a very small percent of the total energy in the system. In order to ameliorate this rather stringent time-step restriction atmospheric scientists have tried various approaches such as using a larger differencing stencil for the gravity wave terms thereby effectively reducing the Courant number, and discretizing the gravity wave terms implicitly in time. We can easily employ the first strategy in our current formulation, that is using a larger differencing stencil for the gravity wave terms, but this is more typically done to avoid the inf-sup (Babuska-Brezzi) condition. However, discretizing the gravity wave terms implicitly in time is a much more effective way of increasing the time-step.

After the gravity wave terms have been successfully discretized the next set of terms responsible for controlling the maximum time-step are the advection terms. In order to use increasingly larger time steps atmospheric scientist have turned to Lagrangian methods for treating these recalcitrant terms. By rewriting the equations in Lagrangian form the troublesome advection terms are absorbed into the total derivative. Thus the equations in this form are now discretized in time along characteristics which results in a much more stable numerical method due to the disappearance of the Courant-Friedrichs-Lewy (CFL) condition.

In the current paper we combine a Lagrangian method with high order basis functions as we showed in [1] and extend this hybrid method to the solution of the hydrostatic atmospheric equations. The allure of this method is that it achieves the same order of accuracy obtained with exponentially high order explicit Eulerian methods [2] while permitting time-steps at least 5 times larger.

2. ATMOSPHERIC EQUATIONS

In this paper we show how to solve the hydrostatic primitive equations which describe the motion of the atmosphere. We assume dry physics (i.e., no physical parameterization) and thus only take into account the dynamical processes. The equations we solve are

$$\frac{\partial \pi}{\partial t} + \boldsymbol{\nabla} \cdot (\pi \boldsymbol{u}) + \frac{\partial}{\partial \sigma}(\pi \dot{\sigma}) = 0 \tag{1}$$

$$\frac{\partial \boldsymbol{u}}{\partial t} + \boldsymbol{u} \cdot \boldsymbol{\nabla} \boldsymbol{u} + \dot{\sigma} \frac{\partial \boldsymbol{u}}{\partial \sigma} = -\frac{2\Omega z}{a^2}(\boldsymbol{x} \times \boldsymbol{u}) - \boldsymbol{\nabla} \varphi - c_p \theta \frac{\partial P}{\partial \pi} \boldsymbol{\nabla} \pi \tag{2}$$

$$\frac{\partial \theta}{\partial t} + \boldsymbol{u} \cdot \boldsymbol{\nabla} \theta + \dot{\sigma} \frac{\partial \theta}{\partial \sigma} = 0 \tag{3}$$

$$\frac{\partial \varphi}{\partial P} = -c_p \theta \tag{4}$$

where

$$\pi = p_s - p_t \ , \ \sigma = \frac{p - p_t}{\pi}$$

and (a, Ω) are the radius and angular rotation of the earth, respectively. The prognostic variables for these equations are $\boldsymbol{q} = (\pi, \boldsymbol{u}, \theta)^T$, while $\dot{\sigma}$ and φ represent diagnostic variables.

3. TEMPORAL DISCRETIZATION

The Lagrangian form of the conservation equations are

$$\frac{d\pi}{dt} = -\pi \left(\boldsymbol{\nabla} \cdot \boldsymbol{u} + \frac{\partial \dot{\sigma}}{\partial \sigma} \right) \tag{5}$$

$$\frac{d\boldsymbol{u}}{dt} = -\frac{2\Omega z}{a^2}(\boldsymbol{x} \times \boldsymbol{u}) - \boldsymbol{\nabla}\varphi - c_p \theta \frac{\partial P}{\partial \pi} \boldsymbol{\nabla}\pi \tag{6}$$

$$\frac{d\theta}{dt} = 0 \tag{7}$$

where the Lagrangian derivative is

$$\frac{d}{dt} = \frac{\partial}{\partial t} + \boldsymbol{u} \cdot \boldsymbol{\nabla}.$$

Discretizing the conservation equations in time by the second order backward difference formula yields

$$\frac{\pi^{n+1} - \frac{4}{3}\pi^{\tilde{n}} + \frac{1}{3}\pi^{\tilde{n}-1}}{\Delta t} = -\frac{2}{3}\pi \left(\boldsymbol{\nabla} \cdot \boldsymbol{u} + \frac{\partial \dot{\sigma}}{\partial \sigma} \right)^{n+1} \tag{8}$$

$$\frac{\boldsymbol{u}^{n+1} - \frac{4}{3}\boldsymbol{u}^{\tilde{n}} + \frac{1}{3}\boldsymbol{u}^{\tilde{n}-1}}{\Delta t} = -\frac{2}{3}\left[\frac{2\Omega z}{a^2}(\boldsymbol{x} \times \boldsymbol{u}) + \boldsymbol{\nabla}\varphi + c_p \theta \frac{\partial P}{\partial \pi} \boldsymbol{\nabla}\pi \right]^{n+1} \tag{9}$$

$$\frac{\theta^{n+1} - \frac{4}{3}\theta^{\tilde{n}} + \frac{1}{3}\theta^{\tilde{n}-1}}{\Delta t} = 0 \tag{10}$$

where the variables $\boldsymbol{q}^{\tilde{n}}$ and $\boldsymbol{q}^{\tilde{n}-1}$ denote Lagrangian departure point values.

3.1. Linearization of the Equations

To avoid having to solve a nonlinear problem we linearize the equations as follows. The surface pressure is linearized about the reference state $\pi^* = 1000$ hPa as such

$$\widehat{\pi} = \pi - \pi^*$$

where $\widehat{\pi}$ now denotes the perturbation surface pressure. In addition, let us introduce the reference potential temperature

$$\theta^* = \frac{T^*}{P(\pi^*)}$$

with $T^* = 300^\circ$ Kelvin. It should be understood that the reference potential temperature is a function of the vertical coordinate σ because the Exner function varies with σ.

3.1.1. Surface Pressure Equation

With the above linearizations the surface pressure equation takes the following form

$$\frac{\widehat{\pi}^{n+1} - \frac{4}{3}\widehat{\pi}^{\tilde{n}} + \frac{1}{3}\widehat{\pi}^{\tilde{n}-1}}{\Delta t} = -\frac{2}{3}\pi^* \left(\boldsymbol{\nabla} \cdot \boldsymbol{u} + \frac{\partial \dot{\sigma}}{\partial \sigma} \right)^{n+1} . \tag{11}$$

3.1.2. Hydrostatic Equation

Beginning with the finite differenced equation for geopotential

$$\varphi_k - \varphi_{k+1} = c_p \theta_k \left(P_{k+1/2} - P_k \right) + c_p \theta_{k+1} \left(P_{k+1} - P_{k+1/2} \right)$$

where $k = 1, ..., N_{lev}$ and N_{lev} represents the number of vertical levels in the model, we can then take a Taylor series expansion about the reference surface pressure π^* and potential temperature θ^* yielding

$$\begin{aligned} \varphi_k - \varphi_{k+1} &= c_p \theta_k \left(P^*_{k+1/2} - P^*_k \right) + c_p \theta_{k+1} \left(P^*_{k+1} - P^*_{k+1/2} \right) \\ &+ c_p \theta^*_k \left(\frac{\partial P^*_{k+1/2}}{\partial \pi} - \frac{\partial P^*_k}{\partial \pi} \right) (\pi - \pi^*) + c_p \theta^*_{k+1} \left(\frac{\partial P^*_{k+1}}{\partial \pi} - \frac{\partial P^*_{k+1/2}}{\partial \pi} \right) (\pi - \pi^*) . \end{aligned} \tag{12}$$

Equation (12) can be written in the matrix form

$$A^{\varphi}_{k,l} \varphi_l = b^{\varphi}_k(\theta) + c^{\varphi}_k \, \widehat{\pi}$$

where

$$b^{\varphi}_k(\theta) = c_p \theta_k \left(P^*_{k+1/2} - P^*_k \right) + c_p \theta_{k+1} \left(P^*_{k+1} - P^*_{k+1/2} \right)$$

and

$$c^{\varphi}_k = c_p \theta^*_k \left(\frac{\partial P^*_{k+1/2}}{\partial \pi} - \frac{\partial P^*_k}{\partial \pi} \right) (\pi - \pi^*) + c_p \theta^*_{k+1} \left(\frac{\partial P^*_{k+1}}{\partial \pi} - \frac{\partial P^*_{k+1/2}}{\partial \pi} \right) (\pi - \pi^*) .$$

This results in the following geopotential gradient

$$\boldsymbol{\nabla} \varphi_k = \boldsymbol{\nabla} \left((A^{\varphi}_{k,l})^{-1} \left[b^{\varphi}_l(\theta) + c^{\varphi}_l \, \widehat{\pi} \right] \right) . \tag{13}$$

3.1.3. Momentum Equations

Linearizing the gradient due to surface pressure yields

$$\left(c_p \theta_k \frac{\partial P_k}{\partial \pi} \boldsymbol{\nabla} \widehat{\pi} \right)^{n+1} = \left(c_p \theta^*_k \frac{\partial P^*_k}{\partial \pi} \boldsymbol{\nabla} \widehat{\pi}^{n+1} \right) .$$

The momentum equations then look as follows

$$\boldsymbol{u}^{n+1} + \frac{2}{3}\Delta t \left(\frac{2\Omega z}{a^2} (\boldsymbol{x} \times \boldsymbol{u}) \right)^{n+1} = \frac{4}{3}\boldsymbol{u}^{\tilde{n}} - \frac{1}{3}\boldsymbol{u}^{\tilde{n}-1} - \frac{2}{3}\Delta t \left[\boldsymbol{\nabla} \varphi^{n+1} + c_p \theta^* \frac{\partial P^*}{\partial \pi} \boldsymbol{\nabla} \widehat{\pi}^{n+1} \right]$$

which in matrix form are

$$A^u \boldsymbol{u}^{n+1}_k = \frac{4}{3}\boldsymbol{u}^{\tilde{n}}_k - \frac{1}{3}\boldsymbol{u}^{\tilde{n}-1}_k - \frac{2}{3}\Delta t \left[\boldsymbol{\nabla} \varphi^{n+1}_k + c_p \theta^*_k \frac{\partial P^*_k}{\partial \pi} \boldsymbol{\nabla} \widehat{\pi}^{n+1} \right] .$$

Substituting the linearized geopotential from Eq. (13) gives

$$\begin{aligned} A^u \boldsymbol{u}_k^{n+1} &= \frac{4}{3}\boldsymbol{u}_k^{\tilde{n}} - \frac{1}{3}\boldsymbol{u}_k^{\tilde{n}-1} \\ &- \frac{2}{3}\Delta t \left[\boldsymbol{\nabla} \left((A^{\varphi}_{k,l})^{-1} \left[b_l^{\varphi}(\theta^{n+1}) + c_l^{\varphi}\, \widehat{\pi}^{n+1} \right] \right) + c_p \theta_k^* \frac{\partial P_k^*}{\partial \pi} \boldsymbol{\nabla} \widehat{\pi}^{n+1} \right] \end{aligned}$$

and inverting yields

$$\boldsymbol{u}_k^{n+1} = (A^u)^{-1} \left[\begin{array}{c} \frac{4}{3}\boldsymbol{u}_k^{\tilde{n}} - \frac{1}{3}\boldsymbol{u}_k^{\tilde{n}-1} - \frac{2}{3}\Delta t \left[\boldsymbol{\nabla} \left((A^{\varphi}_{k,l})^{-1} b_l^{\varphi}(\theta^{n+1}) \right) \right] \\ -\frac{2}{3}\Delta t \left[\boldsymbol{\nabla} \left((A^{\varphi}_{k,l})^{-1} c_l^{\varphi}\, \widehat{\pi}^{n+1} \right) + c_p \theta_k^* \frac{\partial P_k^*}{\partial \pi} \boldsymbol{\nabla} \widehat{\pi}^{n+1} \right] \end{array} \right].$$

Let us now rewrite this more compactly as follows

$$\boldsymbol{u}_k^{n+1} = (A^u)^{-1} \left(b_k^u \left(\theta^{n+1} \right) - \frac{2}{3}\Delta t c_k^u \left(\widehat{\pi}^{n+1} \right) \right) \tag{14}$$

where

$$b_k^u \left(\theta^{n+1} \right) = \frac{4}{3}\boldsymbol{u}_k^{\tilde{n}} - \frac{1}{3}\boldsymbol{u}_k^{\tilde{n}-1} - \frac{2}{3}\Delta t \left[\boldsymbol{\nabla} \left((A^{\varphi}_{k,l})^{-1} b_l^{\varphi}(\theta^{n+1}) \right) \right] \tag{15}$$

and

$$c_k^u \left(\widehat{\pi}^{n+1} \right) = \boldsymbol{\nabla} \left((A^{\varphi}_{k,l})^{-1} c_l^{\varphi}\, \widehat{\pi}^{n+1} \right) + c_p \theta_k^* \frac{\partial P_k^*}{\partial \pi} \boldsymbol{\nabla} \widehat{\pi}^{n+1}. \tag{16}$$

3.2. Calculation of Departure Point Values

The discretization of the hydrostatic primitive equations that we have described so far are complete provided that we have a means of computing the state vector at the departure point values. Below we describe two possible approaches which are rather similar: the semi-Lagrangian method and the Eulerian-Lagrangian method.

3.2.1. Semi-Lagrangian Method

In the semi-Lagrangian method, the departure point values are obtained as follows. We solve the Lagrangian pure advection problem

$$\frac{d\boldsymbol{q}}{dt} = 0 \ \text{ and } \ \frac{d\boldsymbol{x}}{dt} = \boldsymbol{u}. \tag{17}$$

In the current implementation we use a 2nd order Runge-Kutta method to solve the trajectory equation.

3.2.2. Eulerian-Lagrangian Method

Although this method is known in the literature as the operator-integration-factor splitting method (see [6]) we have chosen to refer to it as the Eulerian-Lagrangian method because it represents an Eulerian approximation to the Lagrangian problem. In the Eulerian-Lagrangian method the departure point values $\boldsymbol{q}^{\tilde{n}}$ and $\boldsymbol{q}^{\tilde{n}-1}$ are obtained as follows. We solve the Eulerian pure advection problem

$$\frac{\partial \boldsymbol{q}^k}{\partial \tau} + \boldsymbol{u} \cdot \boldsymbol{\nabla} \boldsymbol{q}^k = 0 \tag{18}$$

with $\boldsymbol{q}(\boldsymbol{x}, t^{\widetilde{n}+1-k}) = \boldsymbol{q}(\boldsymbol{x}, t^{n+1-k})$ where the velocity field $\boldsymbol{u}$ is extrapolated from the known velocity fields at times $n-2$, $n-1$, and n. In the current implementation we use a 2nd order Runge-Kutta method to solve this equation.

4. HELMHOLTZ OPERATOR

In order to solve for the surface pressure we need to integrate Eq. (11) vertically from $\sigma = 0$ to $\sigma = 1$ which yields

$$\sum_{k=1}^{N_{lev}} \frac{\widehat{\pi}^{n+1} - \frac{4}{3}\widehat{\pi}_k^{\widetilde{n}} + \frac{1}{3}\widehat{\pi}_k^{\widetilde{n}-1}}{\Delta t}\Delta\sigma_k = -\frac{2}{3}\pi^* \sum_{k=1}^{N_{lev}} \left(\boldsymbol{\nabla}\cdot\boldsymbol{u}\right)_k^{n+1} \Delta\sigma_k - \frac{2}{3}\pi^* \left[\dot{\sigma}\right]_{\sigma=0}^{\sigma=1}$$

where $\widehat{\pi}^{n+1}$ is purposely not given a vertical level subscript to denote that the arrival surface pressure is only a function of the 2D surface. Using the no-flux boundary condition at the top and bottom of the atmosphere yields

$$\sum_{k=1}^{N_{lev}} \frac{\widehat{\pi}^{n+1} - \frac{4}{3}\widehat{\pi}_k^{\widetilde{n}} + \frac{1}{3}\widehat{\pi}_k^{\widetilde{n}-1}}{\Delta t}\Delta\sigma_k = -\frac{2}{3}\pi^* \sum_{k=1}^{N_{lev}} \left(\boldsymbol{\nabla}\cdot\boldsymbol{u}\right)_k^{n+1} \Delta\sigma_k. \tag{19}$$

Substituting $\boldsymbol{u}^{n+1}$ from Eq. (14) and rearranging gives

$$\sum_{k=1}^{N_{lev}} \widehat{\pi}^{n+1}\Delta\sigma_k = \sum_{k=1}^{N_{lev}} \left\{ \frac{4}{3}\widehat{\pi}_k^{\widetilde{n}} - \frac{1}{3}\widehat{\pi}_k^{\widetilde{n}-1} - \frac{2}{3}\Delta t\pi^*\boldsymbol{\nabla}\cdot\left[(A^u)^{-1}\left(b_k^u\left(\theta^{n+1}\right) - \frac{2}{3}\Delta t c_k^u\left(\widehat{\pi}^{n+1}\right)\right)\right]\right\}\Delta\sigma_k.$$

Substituting for $c_k^u\left(\widehat{\pi}\right)$ from Eq. (16) yields

$$\begin{aligned}
&\sum_{k=1}^{N_{lev}} \left\{ \widehat{\pi}^{n+1} - \frac{4}{9}\Delta t^2\pi^*\boldsymbol{\nabla}\cdot\left[(A^u)^{-1}\left(\boldsymbol{\nabla}\left((A_{k,l}^{\varphi})^{-1}c_l^{\varphi}\,\widehat{\pi}^{n+1}\right) + c_p\theta_k^*\frac{\partial P_k^*}{\partial\pi}\boldsymbol{\nabla}\widehat{\pi}^{n+1}\right)\right]\right\}\Delta\sigma_k = \\
&\sum_{k=1}^{N_{lev}} \left\{ \frac{4}{3}\widehat{\pi}_k^{\widetilde{n}} - \frac{1}{3}\widehat{\pi}_k^{\widetilde{n}-1} - \frac{2}{3}\Delta t\pi^*\boldsymbol{\nabla}\cdot\left((A^u)^{-1}b_k^u\left(\theta^{n+1}\right)\right)\right\}\Delta\sigma_k.
\end{aligned} \tag{20}$$

The interesting result from this linearization is that the terms $(A_{k,l}^{\varphi})^{-1}c_l^{\varphi}$ and $c_p\theta_k^*\frac{\partial P_k^*}{\partial\pi}$ are not functions of the horizontal operators and so they can be factored from the gradient and divergence operators. Doing so yields

$$\begin{aligned}
&\widehat{\pi}^{n+1} - \left[\frac{4}{9}\Delta t^2\pi^*\sum_{k=1}^{N_{lev}}\left((A_{k,l}^{\varphi})^{-1}c_l^{\varphi} + c_p\theta_k^*\frac{\partial P_k^*}{\partial\pi}\right)\Delta\sigma_k\right]\boldsymbol{\nabla}\cdot\left((A^u)^{-1}\boldsymbol{\nabla}\widehat{\pi}^{n+1}\right) = \\
&\sum_{k=1}^{N_{lev}} \left\{ \frac{4}{3}\widehat{\pi}_k^{\widetilde{n}} - \frac{1}{3}\widehat{\pi}_k^{\widetilde{n}-1} - \frac{2}{3}\Delta t\pi^*\boldsymbol{\nabla}\cdot\left((A^u)^{-1}b_k^u\left(\theta^{n+1}\right)\right)\right\}\Delta\sigma_k
\end{aligned} \tag{21}$$

where we have removed $\widehat{\pi}^{n+1}$ from the summation because it is not a function of the vertical coordinate σ. This expression tells us that the first bracketed term on the LHS can be computed once, because it is not a function of time, and then taken as a constant in the solution of the 2D surface pressure Helmholtz equation. To this end, we rewrite the Helmholtz equation as follows

$$\widehat{\pi}^{n+1} - \lambda\boldsymbol{\nabla}\cdot\left((A^u)^{-1}\boldsymbol{\nabla}\widehat{\pi}^{n+1}\right) = b^{\pi} \tag{22}$$

where

$$\lambda = \frac{4}{9}\Delta t^2 \pi^* \sum_{k=1}^{N_{lev}} \left((A^{\varphi}_{k,l})^{-1} c^{\varphi}_l + c_p \theta^*_k \frac{\partial P^*_k}{\partial \pi} \right) \Delta\sigma_k \tag{23}$$

and

$$b^{\pi} = \sum_{k=1}^{N_{lev}} \left\{ \frac{4}{3}\widehat{\pi}^{\widetilde{n}}_k \frac{1}{3}\widehat{\pi}^{\widetilde{n}-1}_k - \frac{2}{3}\Delta t \pi^* \boldsymbol{\nabla} \cdot \left((A^u)^{-1} b^u_k \left(\theta^{n+1} \right) \right) \right\} \Delta\sigma_k. \tag{24}$$

5. GRID GENERATION ON THE SPHERE

Hexahedral (a.k.a. cubic gnomonic) grids are constructed by subdividing the 6 faces of a hexahedron into the desired number of quadrilateral elements, and then mapping these onto the sphere. This approach results in the construction of a hexahedral grid with the following properties

$$\begin{aligned} N_{\mathrm{p}} &= 6(n_H N)^2 + 2 \\ N_{\mathrm{e}} &= 6(n_H)^2 \end{aligned}$$

where N_{p} and N_{e} denote the number of points and elements comprising the grid. The parameter n_H refers to the number of quadrilateral elements in each direction contained in each of the 6 initial faces of the hexahedron and N is the order of the basis functions of each of the elements. The comparable hexahedral resolution to the spectral triangular truncation, T, can be obtained by the expression

$$T = n_H N.$$

Thus to obtain T160 we can use $n_H = 20$ and $N = 8$.

6. RESULTS

6.1. Rossby-Haurwitz Waves

In order to judge the accuracy of SEELAM we have run Rossby-Haurwitz waves numbers one and four and compared the surface pressure of SEELAM with those of NOGAPS [4] for a T160 L24 resolution after 5 day integrations. The SEELAM model uses a time step three times larger than the NOGAPS model for these tests.

Figure 1 shows the wave one results while Fig. 2 shows the wave four results. There are slight differences in the shape of the waves but both models yield the same maximum and minimum contour levels. More importantly both models yield the same phase speeds.

6.2. Jablonowski-Williams Tests

The following two cases represent a new set of tests for judging the accuracy and stability of dynamical cores. These tests are introduced in Jablonowski and Williamson [5].

6.2.1. Balanced Initial State

For this test case, the atmosphere is initially balanced. With the given initial conditions the equations should remain balanced for an indefinite amount of time. Figure 3 shows the normalized surface pressure, π, L_2 error norm as a function of time for a four week period for SEE-AM and SEELAM with T160 horizontal resolution and 24 vertical levels. SEE-AM is the explicit Eulerian version presented in [2]. Note that while the error oscillates with time it remains bounded which confirms that the initial balanced state is maintained by both models. In addition, both models give

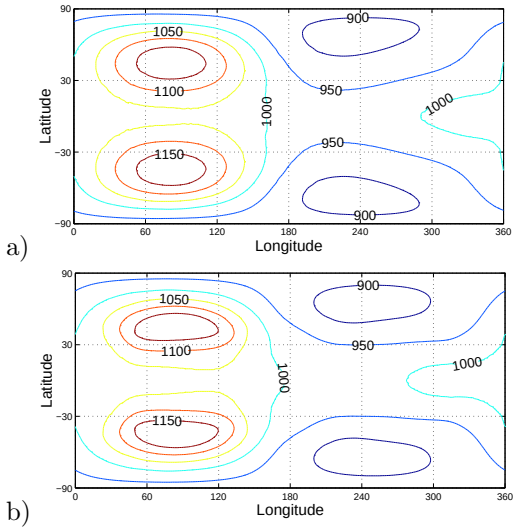

FIG. 1. Rossby-Haurwitz Wave Number 4: The surface pressure (hPa) for a) NOGAPS and b) SEELAM for $T160$ and $N_{\text{lev}} = 24$ for a 5 day integration.

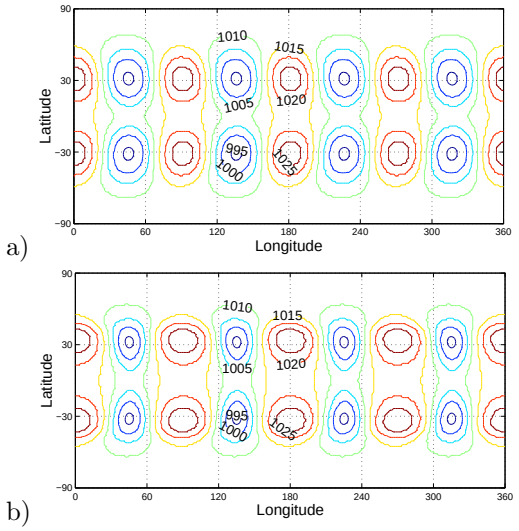

FIG. 2. Rossby-Haurwitz Wave Number 4: The surface pressure (hPa) for a) NOGAPS and b) SEELAM for $T160$ and $N_{\text{lev}} = 24$ for a 5 day integration.

identical errors up to 18 days at which point the models differ but not significantly. This result is perhaps the most encouraging result in the suite because it confirms that the Lagrangian implicit SEELAM is behaving like the explicit Eulerian SEE-AM.

6.2.2. Baroclinic Instability

This case is similar to the balanced initial state except that now a perturbation is added to the initial zonal velocity. This perturbation grows until a baroclinic instability develops and then breaks near day nine. Figure 4 shows the minimum surface pressure p_s as a function of time for SEELAM against various models including the NCAR spectral transform model [3], the NASA Goddard finite

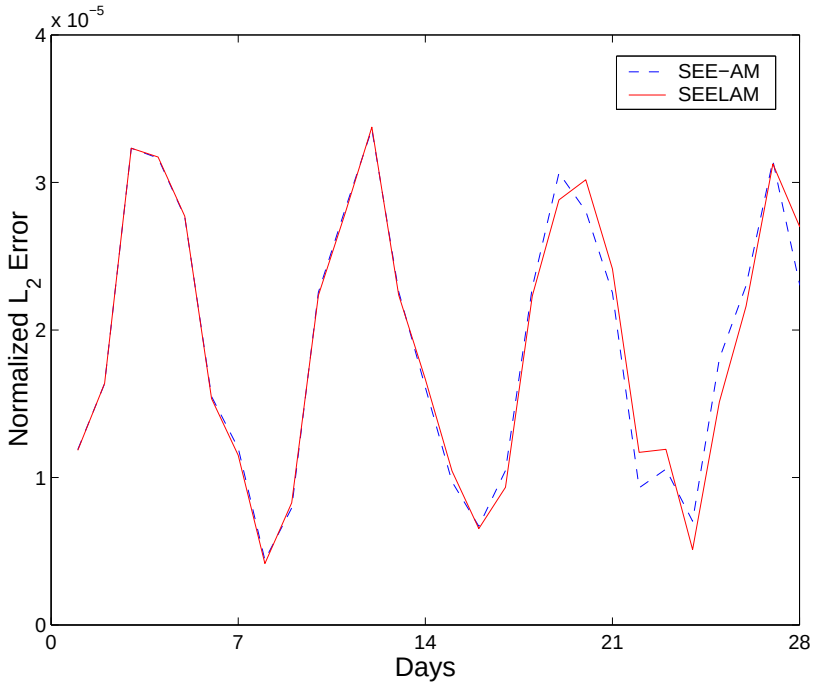

FIG. 3. Jablonowski-Williamson Balanced Initial State: The normalized surface pressure, π, L_2 error as a function of days for SEE-AM (dashed line) and SEELAM (solid line) for T160 ($n_H = 20$ and $N = 8$) with 24 vertical levels.

volume model [10], and the German Weather Service icosahedral finite difference model [7] which we denote as GME; the results of the latter three models are courtesy of Christiane Jablonowski. The results in Fig. 4 are summarized as follows. SEELAM compares well with the three established models. The lower order NASA and GME models give very similar results. Finally, the higher order NCAR and SEELAM models compare extremely well with each other.

7. CONCLUSION

A new dynamical core for numerical weather prediction (NWP) based on the spectral element Eulerian-Lagrangian (SEEL) method is presented. In a previous paper [2] we showed the advantages of using spectral elements in 3D Cartesian coordinates. In this paper we have extended the explicit Eulerian method described in [2] to an implicit Lagrangian method. The advantage of using the implicit Eulerian-Lagrangian method is that it permits time steps 5 times larger than the explicit Eulerian method. This increase in permissible time step should translate into increased efficiency of the model. While the SEELAM model has not yet been fully tested it has passed its first four tests demonstrating that it behaves similarly to well-established climate and weather prediction models. These models include: the U.S. Navy's NWP model and the NCAR climate model. In order to become competitive with these well-established models the iterative solvers for inverting the resulting Helmholtz operator must be fully optimized. This is the topic of future work.

ACKNOWLEDGMENT

This work was supported by the Office of Naval Research through program element PE-0602435N. The author would like to thank Paul Fischer for the use of his GMRES solver.

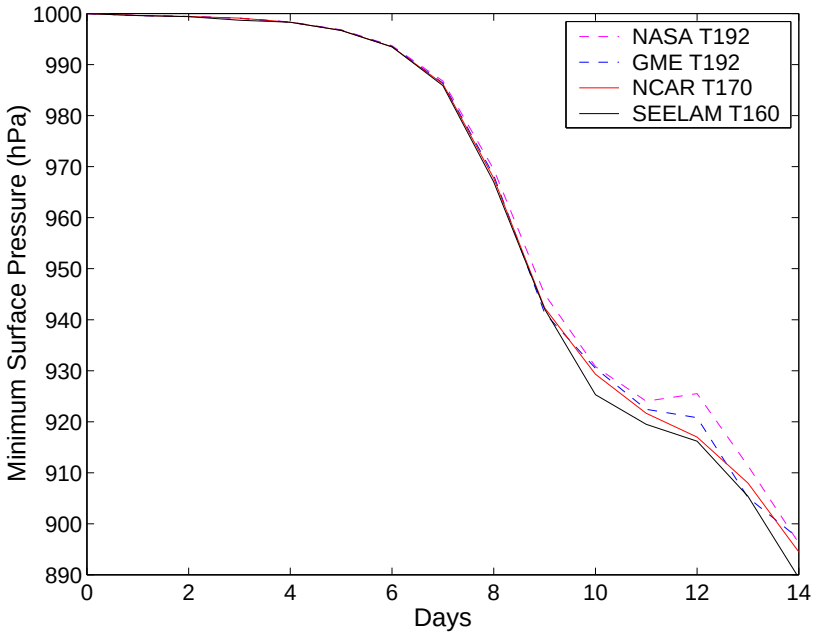

FIG. 4. Jablonowski-Williamson Baroclinic Instability: The minimum surface pressure (hPa) as a function of days for the NASA (finite volume), GME (finite-difference), NCAR (spectral transform), and SEELAM (spectral element with $n_H = 20$ and $N = 8$) models using 26 vertical levels. (The data for the first three models are courtesy of Christiane Jablonowski.)

REFERENCES

1. F.X. Giraldo and J.B. Perot, A spectral element semi-Lagrangian method for the spherical shallow water equations, *Journal of Computational Physics* in review (2003).
2. F.X. Giraldo and T.E. Rosmond, A scalable spectral element Eulerian atmospheric model (SEE-AM) for NWP: dynamical core tests, *Monthly Weather Review* in review (2003).
3. J.J. Hack, B.A. Boville, B.P. Briegleb, J.T. Kiehl, P.J. Rasch, and D.L. Williamson, Description of the NCAR community climate model (CCM2), NCAR Technical Note NCAR/TN-382+STR. (1992).
4. T.F. Hogan and T.E. Rosmond, The description of the Navy Global Operational Prediction System's spectral forecast model, *Monthly Weather Review* **119**, 1786-1815 (1991).
5. C. Jablonowski and D.L. Williamson, Baroclinic instability test with two jets in the midlatitudes, Abstracts, *The 2002 Workshop on the Solution of Partial Differential Equations on the Sphere*, Toronto, Canada, 10-10 (2002).
6. Y. Maday, A.T. Patera, and E.M. Ronquist, An operator-integration-factor splitting method for time-dependent problems: applications to incompressible fluid flow, *Journal of Scientific Computing* **5**, 263-292 (1990).
7. D. Majewski, D. Liermann, P. Prohl, R. Ritter, M. Buchhold, T. Hanisch, G. Paul, W. Wergen, and J. Baumgardner, The operational global icosahedral-hexahedral gridpoint model GME: description and high-resolution tests, *Monthly Weather Review* **130**, 319-338 (2002).
8. J.G. Sela J.G., Spectral modeling at the National Meteorlogical Center, *Monthly Weather Review* **108**, 1279-1292 (1980).
9. A.J. Simmons, D.M. Burridge, M. Jarraud, C. Girard, and W. Wergen, The ECMWF medium-range prediction models development of the numerical formulations and the impact of increased resolution, *Meteorology and Atmospheric Physics* **40**, 28-60 (1989).
10. K.S. Yeh, S.J. Lin, and R.B. Rood, Applying local discretization methods in the NASA finite-volume general circulation model, *Computing in Science and Engineering* **4**, 49-54 (2002).